https://doi.org/10.1016/j.powtec.2017.10.012

This is the Pre-Published Version.

Nanoparticle Formation and Growth in Turbulent Flows using the Bimodal TEMOM

Tat Leung Chan*, Shuyuan Liu, Yan Yue

Department of Mechanical Engineering, The Hong Kong Polytechnic University,

Hung Hom, Kowloon, Hong Kong

*Corresponding author and E-mail address: mmtlchan@polyu.edu.hk (T.L. Chan)

Abstract

A developed bimodal Taylor-series expansion method of moments (B-TEMOM) is first coupled with a large eddy simulation (LES) model to investigate nanoparticle formation and subsequent growth due to nucleation, coagulation and condensation processes in turbulent flows. An incompressible gas mixture containing sulfuric acid and water vapor is injected into a stationary flow field with background aerosols. The spatial and temporal particle size distribution (PSD), particle number and mass concentrations, and competition between the formation of primary and secondary particles in turbulent flows are studied. The instantaneous results demonstrate that the large coherent structures strongly affect the particle number and mass concentration distributions as well as particle polydispersity. This finding also verifies that the coherent structures enhance diffusion in the flows and finally increases particle transfer between the two modes of particles. Furthermore, the numerical simulation results obtained by the B-TEMOM are validated with those obtained by the sectional method with excellent agreement.

Keywords: Bimodal Taylor-series expansion method of moments (B-TEMOM), Particle size distribution, Large eddy simulation, Nanoparticle formation and growth

© 2017. This manuscript version is made available under the CC-BY-NC-ND 4.0 license http://creativecommons.org/licenses/by-nc-nd/4.0/.

Nomenclature

A	constant (= 1.591)	**Greek letters**	
B_1,B_2	dimensionless particle fractal collision coefficient	β	particle collision kernel
d	particle diameter, nm	λ	mean free path of molecular air, m
D_f	dimensionless particle fractal dimension	ρ	density, kg/m^3
f	the reciprocal of D_f	μ	dynamic viscosity, Pa·s
k_B	Boltzmann constant, J/K	ϕ	Cunningham correction factor, dimensionless
k^*	number of sulfuric acid molecules in the critical particle	η	the number concentration of molecular sulfuric acid, #/m^3
M_k, L_k	kth order moment of Mode 1 and Mode 2	Γ	diffusion coefficient, m^2/s
m_k,l_k	kth order moment of Mode 1 and Mode 2	τ, T	dimensionless time
n, p	particle number concentration, #/m^3	ξ, ζ, ς, ϑ	combination of moments
n_s	number of sulfuric acid molecules	δ_{lg}, δ_{mg}	geometric mean deviation, dimensionless
R^*	dimensionless particle generation rate	**Abbreviation**	
R	particle generation rate, #/m^3	B-TEMOM	bimodal Taylor-series expansion method of moments
$\overline{s}_{ij}$	the filtration rate of strain tensor in the LES model	LES	large eddy simulation
T	dimensionless time	PSD	particle size distribution
T_k	temperature, K	PBE	population balance equation
T_{kk}, $T_{i,j}$	sub-grid scale stress tensor	SM	sectional method
u_j	fluid velocity, m/s	CFD	computational fluid dynamics
$\overline{u}_i$	velocity after filtering, m/s	log MM	log-normal method of moments
u_m	the jet velocity in the centerline of the nozzle, m/s	QMOM	quadrature method of moments
v	particle volume, m^3	QBMOM	quadrature-based method of moments
v_{p0}	volume of primary particles, m^3	TEMOM	Taylor-series expansion method of moments
w	half width of the nozzle, m	bi-MD	bi-Megardis & Dobbins
x,y	the coordinates in horizontal and vertical directions, m	RANS	Reynolds averaged Navier-Stokes method

1. Introduction

In the production of high purity particles by gas-phase chemical reaction systems, such as the synthesis of TiO_2 and silica particles through flame combustion [1], the particle size distribution (PSD) can be described as a bimodal model [2-6]. The dynamic process of a bimodal model can be simply described as follows: The PSD is divided into two modes, i.e. the accumulation mode (large particle) and the nucleation mode (small particle). The intra-mode collision between two small particles generates another larger mode. During inter-mode collisions, the smaller particles will adsorb on the surface of relatively larger particles, which mainly results in the formation of larger particles belonging to the accumulation mode. Similarly, this phenomenon also occurs in the field of the ultrafine particle emission control. To control the emissions of ultrafine particles, especially heavy metal emissions, a very promising method to remove the ultrafine particle has been through the introduction of larger particles [7]. The removal of dust or aerosols by raindrops and water vapor [7-10], which can also be investigated using a bimodal model. In these aerosol systems, the evolution of different PSDs can be theoretically described as a population balance equation (PBE) based on the Smoluchowski's equation [11], which is greatly influenced by Brownian coagulation. The PBE is an integral-differential equation involving Brownian coagulation, but it cannot be solved analytically without any prior assumptions. Fortunately, great contributions have been made by eminent researchers to obtain the solutions of PBEs. Three main numerical methods with their own advantages and disadvantages can be used to obtain the corresponding numerical solutions to PBEs as an alternative to analytical solutions. These three methods include the sectional method (SM) [12-14], the method of moment [6, 15-23], and the Monte Carlo method

[24-27]. Compared with the other two numerical methods, the method of moments has relatively simpler mathematical forms for implementation and lower computational cost (e.g., computational time, computer memory, etc.), which is inherently natural to be coupled with computational fluid dynamics (CFD) codes [2,6,16,20,22,23]. Many types of the method of moments exist, including the log-normal method of moments (log MM) [17], the quadrature method of moments (QMOM) [18], the quadrature-based moments methods (QBMM), such as QMOM, DQMOM, HMOM and EQMOM [28-33], and Taylor-series expansion method of moments (TEMOM) [20,34]. The well-developed TEMOM, which is the basis of the B-TEMOM [6] in the present study, will be modified when the bimodal size distributed aerosol is dealt with.

In atmospheric and environmental science as well as aerosol-related engineering applications, the fine particles-dominated size range and the relatively larger particles-dominated size range are usually separated, which allows for the treatment of dividing the whole size distribution into several separated sub-size distributions. Several bimodal methods based on the methods of moments have been developed to resolve practical aerosol-related problems [4,6,30,35]. Megardis & Dobbins (1990) proposed a method of moments called the bi-Megardis & Dobbins (i.e., bi-M&D) model [35], in which a bimodal log-normal integral equation is used to solve aerosol-related problems, including the processes of particle formation and coagulation. According to [35], the entire PSD was artificially divided into large and small size sections, i.e., nucleation and accumulation modes. Both the two modes were assumed to be log normal PSD. It is shown that the bi-M&D is more suitable for solving problems with bimodal PSD than the method of moments with a unimodal model. Whitby & McMurry (1997) proposed the modal aerosol dynamics method [36], in which each mode of an aerosol system is treated as a separated PSD. Jeong & Choi (2005) also studied bimodal aerosol systems undergoing nucleation and coagulation by applying the log-normal method of moments into the bimodal problems [4]. Two discrete monodisperse modes were used to describe the bimodal PSD and the log-normal function for nucleation and accumulation modes. Compared with the work of Megardis & Dobbins (1990) [35], the bimodal log-normal method of moment [4] demonstrates good agreement and better performance than the bi-M&D and convectional unimodal log-normal models. Although all of these bimodal moment methods mentioned above have been applied to specific aerosol-related problems with high computational accuracy and efficiency, they all require a prior PSD assumption, which restricts the application scope of these bimodal methods of moment.

To overcome the existing shortcoming of the method of moments that requires an assumption of a log normal PSD, McGraw (1997) developed the quadrature method of moments (QMOM) [19]. Because of the absence of the log-normal PSD assumption, the QMOM was verified to have a broader scope of application (McGraw 1997) than the log MM [17]. The QMOM was further developed by following researchers and several variants of the QMOM appear, including direct QMOM, hybrid MOM and extended QMOM [28,29,33]. The QMOM requires twice the number of quadrature points and product-difference algorithm calculation, which leads to a lower computational efficiency than the log MM. The QMOM's efficiency is increased in its improved version, i.e. direct QMOM [28], in which no product-difference algorithm calculation is required. Yu et al. (2008) developed a new Taylor-series expansion method of moments (TEMOM) [20], in which the closure function for *k*-the moments was established on the basis of Taylor-series expansion technique. The coagulation kernel that needs to be addressed in the TMEOM is different from Frenklach and Harris' Taylor series moments method [37]. In Frenklach and Harris' scheme [37], the coagulation kernel needs to be put out from integral entity and then to be approximated with 2-th Taylor series expansion, while in Yu et al.'s TEMOM, the Taylor expansion technique was used to establish a closure function with respect to *k*-th moments [20]. This TEMOM has the similar computational efficiency to the log MM, but a broader scope of applications because the number of equations to be solved is equal to the number of physical variables. Verification of the computational accuracy and efficiency by comparing with the QMOM, log MM and SM [20,34] shows that TEMOM is a reliable and promising method. The TEMOM was also verified to have higher accuracy as the fractional moment sequence type is used [38]. To further extend the application scope from unimodal to bimodal aerosol dynamics, Yu & Chan (2015) developed a new bimodal Taylor-series expansion method of moments (B-TEMOM) by constructing the bimodal governing equations to solve the bimodal aerosol problems [6]. By comparing with the results obtained from the bimodal QMOM and bimodal log MM, the B-TEMOM shows an capability in obtaining the first three moments and standard geometric deviation [6]. The results of B-TEMOM in the continuum-clip regime in which Brownian coagulation process occurs indicates that it is a reliable method for the solution of bimodal aerosol dynamics.

Multidimensional particle dynamics involving nucleation, coagulation, breakage, and surface growth processes coupled with convection, diffusion and thermophoresis and transport processes can be described by PBE together with the governing equations in computational fluid dynamics (CFD) [39-41], i.e., the Navier-Stokes equations. The commonly used methods to investigate the evolution of particle dynamics in turbulent flows include the Reynolds-averaged Navier-Stokes (RANS) and large eddy simulation (LES). RANS is the most popular method because of its satisfactory efficiency and feasibility in obtaining the results of specific variables. Although the detailed information, such as a small vortex, may significantly affect the growth of particles, the detailed information on turbulent flows and the evolution of particle properties with time cannot be provided by RANS, as it is a time-averaged method. On the other hand, the LES method can capture particle dynamics and the detailed information of turbulent flows with high spatial and temporal resolution at acceptable computational cost. In the LES, the large-scale variables are calculated directly and turbulence model is used to simulate the small-scale variables, which guarantees both high computational accuracy and efficiency. Because of its advantages in computational efficiency and accuracy, LES is commonly used to investigate the evolution of particles in practical turbulent flows at a proper computational cost. The LES method can show the details and crucial information of the desired variables, and the coherent structures of particles can also be well exhibited, as the coagulation and growth processes of particles are greatly affected by turbulent shear flow.

The computational accuracy and efficiency of B-TEMOM has recently been verified in our previous study [6]. B-TEMOM combined with the LES approach provides a very promising numerical method to predict or evaluate bimodal aerosol-related problems. Because of the simplicity of B-TEMOM in the mathematical approach, it is extremely easy to be coupled with CFD to investigate specific aerosol-related problems. In the present study, a series of simulations is performed using a combined B-TEMOM with the LES approach in a water-sulfuric acid system with a planar jet flow. Two modes of particles (i.e., Mode 1 and Mode 2) are considered in the present study. The difference of Mode 1 and Mode 2 lies in their sources and particle size ranges. Particles of Mode 1 refer to particles in the surrounding environment (i.e., background particles) with average diameter larger than 100 nm. Particles of Mode 2 refer to particles generated by homogeneous nucleation (i.e., exhaust particles) with average diameter less than 10 nm. The term "particle" in the present study refers to the fractal agglomerates whose diameter is defined as the collision geometric mean diameter of agglomerates. The B-TEMOM model is used for the particle formation and subsequent growth in turbulent flows. The particle dynamics including nucleation, coagulation and growth are examined.

2 Numerical Methodology

2.1 Fluid simulation by LES method

The basic concept of large eddy simulation (LES) is to consider the fluid flow as two parts: the first part is the large-scale structure, which is significantly affected by the turbulence, and the other consists of a small-scale isotropic structure. The governing equations of incompressible flow are decomposed by large eddy simulation, and the momentum and continuity equations obtained from the Navier-Strokes equation are as follows:

$$\frac{\partial \overline{u_\mathrm{i}}}{\partial x_\mathrm{i}} = 0 \tag{1}$$

$$\frac{\partial \overline{u_i}}{\partial t} + u_i \frac{\partial \overline{u_i}}{\partial x_j} = -\frac{1}{\rho}\frac{\partial \overline{p}}{\partial x_i} + \frac{\partial}{\partial x_j}\left(\frac{\mu}{\rho}\frac{\partial \overline{u_i}}{\partial x_j} + T_{ij}\right) \tag{2}$$

where $\overline{u_i}$ is the velocity after filtering, $\overline{p}$ is the pressure after filtering, μ is the dynamic viscosity of the fluid, ρ is the gas density, which can be considered as a constant in the incompressible flow, and i and j are equal to 1 and 2, respectively; T_{ij} is the sub-grid size (SGS) stress tensor. The Smagorinsky-Lily model is used for modeling the sub-grid size as follows:

$$T_{ij} - \frac{1}{3} T_{kk}\delta_{ij} = 2 v_t \overline{s_{ij}} \tag{3}$$

where v_t is the viscosity of the sub-grid size; T_{kk} is the isotropic sub-grid scale stress tensor; $\overline{s_{ij}}$ is the filtration rate strain tensor.

2.2 Particle field

Similar to the velocity shown in Section 2.1, the general dynamics equations (GDEs) accounting for characterizing the evolution of particle dynamics should be also filtered when coupled with the LES. On the basis of the Smoluchowski mean-field theory and the derivation in [6], the transformed ordinary differential equations for bimodal method of moments can be expressed as follows:

$$\frac{dm_k}{dt} + \frac{\partial\left(u_j + u_{(th)j}\right)m_k}{\partial_{x_j}} - \frac{\partial}{\partial x_j}\left(\Gamma \frac{\partial m_k}{\partial x_j}\right) = \underbrace{\frac{1}{2}\int_0^\infty \int_0^\infty \left[(v_c + v_c')^k - v_c^k - v_c'^k\right] \beta(v_c, v_c') n(v_c, t) n(v_c', t) dv_c dv_c'}_{\text{Within Mode 1}}$$

$$+ \underbrace{\int_0^\infty \int_0^\infty \left[(v + v')^k - v^k\right] \beta(v_c, v_c') n(v_c, t) p(v_c', t) dv_c dv_c'}_{\text{Between Mode 1 and Mode 2}} + k B_1 \eta m_{k-1/3} \alpha \tag{4a}$$

$$\frac{dl_k}{dt}+\frac{\partial(u_j+u_{(th)j})l_k}{\partial x_j}-\frac{\partial}{\partial x_j}\left(\Gamma\frac{\partial l_k}{\partial x_j}\right)=\underbrace{\frac{1}{2}\int_0^\infty\int_0^\infty[(v_c+v_c')^k--v_c^k-v_c'^k]\beta(v_c,v_c')p(v_c,t)p(v_c',t)\,dv_c dv_c'}_{\text{Within Mode 2}}$$

$$-\underbrace{\int_0^\infty\int_0^\infty v_c'^k\beta(v_c,v_c')n(v_c,t)p(v_c',t)dv_c dv_c'}_{\text{Between Mode 1 and Mode 2}}+J(\upsilon^*)\upsilon^{*k}+kB_1\eta l_{k\text{-}1/3}\alpha \qquad (4b)$$

On the right hand side of Eq. (4a), the first and second terms represent the variations of particle number density caused by intra-mode coagulation of Mode 1 and inter-mode coagulation between Mode 1 and Mode 2, respectively. Similarly, on the right hand side of Eq. (4b), the first and second terms are the variations of particle number density as a result of intra-mode coagulation of Mode 2 and inter-mode coagulation between Mode 1 and Mode 2, respectively. The *k*th order moments, m_k and l_k are defined as,

$$m_k=\int_0^\infty v^k n(v)\mathrm{d}v \qquad (5a)$$

$$l_k=\int_0^\infty v^k p(v)\mathrm{d}v \qquad (5b)$$

The collision kernel of the continuum plus near-continuum regime, which represents the coagulation effect of particles is calculated as follows [6]:

$$\beta(v_c,v_c')=B_2\{(\frac{1}{v^f}+\frac{1}{v'^f})(v^f+v'^f)+\phi v_{p0}^{f\text{-}\frac{1}{3}}(\frac{1}{v^{2f}}+\frac{1}{v'^{2f}})(v^f+v'^f)\} \qquad (6)$$

The general process of the method of moments is that the PBE with particle number density needs to be transformed into ordinary differential equations (ODEs) of moments. Moment transformation is realized by multiplying the PBE by v^k and then integrating over the entire PSD. If only the first three moments are considered, the ODEs of moments after transforming can be expressed as follows:

$$\left\{\begin{array}{l}
\dfrac{dm_0}{d(B_2t)} = -\dfrac{\partial\left(u_j+u_{(th)j}\right)m_0}{\partial_{x_j}} + \dfrac{\partial}{\partial x_j}\left(\Gamma\dfrac{\partial m_0}{\partial x_j}\right) - \dfrac{1}{2}\left[\xi_1{}^{*} + \varnothing v_{p0}{}^{f-\frac{1}{3}}\xi_2{}^{*}\right] \\
\dfrac{dm_1}{d(B_2t)} = -\dfrac{\partial\left(u_j+u_{(th)j}\right)m_1}{\partial_{x_j}} + \dfrac{\partial}{\partial x_j}\left(\Gamma\dfrac{\partial m_1}{\partial x_j}\right) + \left[\eta_1{}^{**} + \varnothing v_{p0}{}^{f-\frac{1}{3}}\eta_2{}^{**}\right] + \left(\dfrac{B_1}{B_2}\right) \\
\dfrac{dm_2}{d(B_2t)} = -\dfrac{\partial\left(u_j+u_{(th)j}\right)m_2}{\partial_{x_j}} + \dfrac{\partial}{\partial x_j}\left(\Gamma\dfrac{\partial m_2}{\partial x_j}\right) + \dfrac{1}{2}\left[\zeta_1{}^{*} + \varnothing v_{p0}{}^{f-\frac{1}{3}}\zeta_2{}^{*}\right] \\
\qquad + \left[\vartheta_1{}^{**} + \vartheta_2{}^{**}\varnothing v_{p0}{}^{f-\frac{1}{3}}\right] + 2\left(\dfrac{B_1}{B_2}\right)\eta m_{\frac{5}{3}}\alpha \\
\dfrac{dl_0}{d(B_2t)} = -\dfrac{\partial(u_j+u_{(th)j})l_0}{\partial x_j} + \dfrac{\partial}{\partial x_j}\left(\Gamma\dfrac{\partial l_0}{\partial x_j}\right) - \dfrac{1}{2}\left[\xi_1{}^{*'} + \varnothing v_{p0}{}^{f-\frac{1}{3}}\xi_2{}^{*'}\right] \\
\qquad - \left[\xi_1{}^{**} + \varnothing v_{p0}{}^{f-\frac{1}{3}}\xi_2{}^{**}\right] + J\left(\upsilon^{*}\right) \\
\dfrac{dl_1}{d(B_2t)} = -\dfrac{\partial(u_j+u_{(th)j})l_1}{\partial x_j} + \dfrac{\partial}{\partial x_j}\left(\Gamma\dfrac{\partial l_1}{\partial x_j}\right) - \left[\eta_1{}^{**} + \varnothing v_{p0}{}^{f-\frac{1}{3}}\eta_2{}^{**}\right] \\
\qquad - \left[\xi_1{}^{**} + \varnothing v_{p0}{}^{f-\frac{1}{3}}\xi_2{}^{**}\right] + J\left(\upsilon^{*}\right) \\
\dfrac{dl_2}{d(B_2t)} = -\dfrac{\partial\left(u_j+u_{(th)j}\right)l_2}{\partial x_j} + \dfrac{\partial}{\partial x_j}\left(\Gamma\dfrac{\partial l_2}{\partial x_j}\right) + \dfrac{1}{2}\left[\zeta_1{}^{*'} + \varnothing v_{p0}{}^{f-\frac{1}{3}}\zeta_2{}^{*'}\right] \\
\qquad - \left[\varsigma_1{}^{**} + \varsigma_2{}^{**}\varnothing v_{p0}{}^{f-\frac{1}{3}}\right] + J\left(\upsilon^{*}\right)\left(\dfrac{\upsilon^{*}}{\upsilon_w}\right)^2\alpha + 2\left(\dfrac{B_1}{B_2}\right)\eta l_{\frac{5}{3}}
\end{array}\right. \tag{7}$$

where

$$\xi_1{}^{*} = 2m_0m_0 + m_fm_{-f} + m_{-f}m_f$$

$$\xi_2{}^{*} = m_0m_{-f} + m_fm_{-2f} + m_fm_{-2f} + m_0m_{-f}$$

$$\xi_1{}^{*}{}' = 2l_0l_0 + l_fl_{-f} + l_{-f}l_f$$

$$\xi_2{}^{*}{}' = l_0l_{-f} + l_fl_{-2f} + l_fl_{-2f} + l_0l_{-f}$$

$$\xi_1{}^{**} = 2m_0l_0 + m_fl_{-f} + m_{-f}l_f$$

$\xi_2^{**}=m_0l_{-f}+m_fl_{-2f}+l_fm_{-2f}+l_0m_{-f}$

$\eta_1^{**}=2m_0l_1+m_fl_{-f+1}+m_{-f}l_{f+1}$

$\eta_2^{**}=m_{-f}l_1+m_fl_{-2f+1}+m_{-2f}l_{f+1}+m_0l_{-f+1}$

$\zeta_1^{*}=4m_1m_1+2m_{1+f}m_{1-f}+2m_{1+f}m_{1-f}$

$\zeta_2^{*}=2m_{1-f}m_1+2m_{1+f}m_{1-2f}+2m_{1-2f}m_{1+f}+2m_1m_{1-f}$

$\varsigma_1^{**}=2m_0l_2+m_fl_{2-f}+m_{-f}l_{f+2}$

$\varsigma_2^{**}=m_{-f}l_2+m_fl_{2-2f}+m_{-2f}l_{2+f}+m_0l_{2-f}$

$\zeta_1^{*}{}'=4l_1l_1+2l_{1+f}l_{1-f}+2l_{1+f}l_{1-f}$

$\zeta_2^{*}{}'=2l_{1-f}l_1+2l_{1+f}l_{1-2f}+2l_{1-2f}l_{1+f}+2l_1l_{1-f}$

$\zeta_1^{**}=4m_1l_1+2m_{1+f}l_{1-f}+2m_{1-f}l_{1+f}$

$\zeta_2^{**}=2m_{1-f}l_1+2m_{1-2f}l_{1+f}+2m_{1+f}l_{1-2f}+2m_1l_{1-f}$

$\vartheta_1^{**}=\varsigma_1^{**}+\zeta_1^{**}$

$\vartheta_2^{**}=\varsigma_2^{**}+\zeta_2^{**}$

There are still some fractal-order moment variables in Eq. (7). To achieve closure of the ODEs of moments, the fractal order has to be transformed into an integer order moment. By introducing the Taylor-series expansion, the relevant closure equation can be expressed as follows:

$$m_k=\left(\frac{u_m{}^{k\text{-}2}k^2}{2}-\frac{u_m{}^{k\text{-}2}k}{2}\right)m_2+\left(-u_m{}^{k\text{-}1}k^2+2u_m{}^{k\text{-}1}k\right)m_1+\left(u_m{}^k+\frac{u_m{}^kk^2}{2}-\frac{3u_m{}^kk}{2}\right)m_0 \tag{8}$$

$$l_k=\left(\frac{u_l{}^{k\text{-}2}k^2}{2}-\frac{u_l{}^{k\text{-}2}k}{2}\right)l_2+\left(-u_l{}^{k\text{-}1}k^2+2u_l{}^{k\text{-}1}k\right)l_1+\left(u_l{}^k+\frac{u_l{}^kk^2}{2}-\frac{3u_l{}^kk}{2}\right)l_0 \tag{9}$$

where u_m and u_l represent the Taylor-expansion point of different modes. In the present study, the Taylor-expansion point is the same as that determined in [6] in Mode 1, $u_m = \frac{m_1}{m_0}$, and in Mode 2, $u_l = \frac{l_1}{l_0}$.

If the dimensionalized moment equations are used, the numerical uncertainty usually happens due to extremely huge difference in values among traced moments. To overcome the shortcoming of dimensionalized moment equations, the non-dimensionalized moment equations are further implemented. In the present study, the non-dimensionalization method is similar to the methods used in the work of Pratsinis et al. (1988) [2], as listed in Table 1.

Table 1 Non-dimensional terms used in the present study.

The non-dimensionalized moment equations for the particle field are given as follows:

$$\begin{cases} \dfrac{dm_0}{d(B_2t)} = -\dfrac{\partial\left(u_j+u_{(th)j}\right)m_0}{\partial_{x_j}} + \dfrac{\partial}{\partial x_j}\left(\Gamma\dfrac{\partial m_0}{\partial x_j}\right) - \dfrac{1}{2}\left[{\xi_1}^{*} + {\varnothing v_{p0}}^{f-\frac{1}{3}}{\xi_2}^{*}\right] \\ \dfrac{dm_1}{d(B_2t)} = -\dfrac{\partial\left(u_j+u_{(th)j}\right)m_1}{\partial_{x_j}} + \dfrac{\partial}{\partial x_j}\left(\Gamma\dfrac{\partial m_1}{\partial x_j}\right) + \left[{\eta_1}^{**} + {\varnothing v_{p0}}^{f-\frac{1}{3}}{\eta_2}^{**}\right] + \left(\dfrac{B_1}{B_2}\right) \\ \dfrac{dm_2}{d(B_2t)} = -\dfrac{\partial\left(u_j+u_{(th)j}\right)m_2}{\partial_{x_j}} + \dfrac{\partial}{\partial x_j}\left(\Gamma\dfrac{\partial m_2}{\partial x_j}\right) + \dfrac{1}{2}\left[{\zeta_1}^{*} + {\varnothing v_{p0}}^{f-\frac{1}{3}}{\zeta_2}^{*}\right] \\ \qquad + \left[{\vartheta_1}^{**} + {\vartheta_2}^{**}{\varnothing v_{p0}}^{f-\frac{1}{3}}\right] + 2\left(\dfrac{B_1}{B_2}\right)\eta m_{\frac{5}{3}}\alpha \\ \dfrac{dl_0}{d(B_2t)} = -\dfrac{\partial(u_j+u_{(th)j})l_0}{\partial x_j} + \dfrac{\partial}{\partial x_j}\left(\Gamma\dfrac{\partial l_0}{\partial x_j}\right) - \dfrac{1}{2}\left[{\xi_1}^{*'} + {\varnothing v_{p0}}^{f-\frac{1}{3}}{\xi_2}^{*'}\right] \\ \qquad - \left[{\xi_1}^{**} + {\varnothing v_{p0}}^{f-\frac{1}{3}}{\xi_2}^{**}\right] + J\left(\upsilon^{*}\right) \\ \dfrac{dl_1}{d(B_2t)} = -\dfrac{\partial(u_j+u_{(th)j})l_1}{\partial x_j} + \dfrac{\partial}{\partial x_j}\left(\Gamma\dfrac{\partial l_1}{\partial x_j}\right) - \left[{\eta_1}^{**} + {\varnothing v_{p0}}^{f-\frac{1}{3}}{\eta_2}^{**}\right] \\ \qquad - \left[{\xi_1}^{**} + {\varnothing v_{p0}}^{f-\frac{1}{3}}{\xi_2}^{**}\right] + J\left(\upsilon^{*}\right) \\ \dfrac{dl_2}{d(B_2t)} = -\dfrac{\partial\left(u_j+u_{(th)j}\right)l_2}{\partial x_j} + \dfrac{\partial}{\partial x_j}\left(\Gamma\dfrac{\partial l_2}{\partial x_j}\right) + \dfrac{1}{2}\left[{\zeta_1}^{*'} + {\varnothing v_{p0}}^{f-\frac{1}{3}}{\zeta_2}^{*'}\right] \\ \qquad - \left[{\varsigma_1}^{**} + {\varsigma_2}^{**}{\varnothing v_{p0}}^{f-\frac{1}{3}}\right] + J\left(\upsilon^{*}\right)\left(\dfrac{\upsilon^{*}}{\upsilon_w}\right)^2\alpha + 2\left(\dfrac{B_1}{B_2}\right)\eta l_{\frac{5}{3}} \end{cases} \tag{10}$$

where

$${\xi_1}^{*} = 2m_0m_0 + m_f m_{-f} + m_{-f} m_f$$

$${\xi_2}^{*} = m_0m_{-f} + m_f m_{-2f} + m_f m_{-2f} + m_0m_{-f}$$

$${\xi_1}^{*}{}' = 2l_0l_0 + l_f l_{-f} + l_{-f} l_f$$

$${\xi_2}^{*}{}' = l_0\, l_{-f} + l_f\, l_{-2f} + l_f\, l_{-2f} + l_0\, l_{-f}$$

$${\xi_1}^{**} = 2m_0l_0 + m_f l_{-f} + m_{-f} l_f$$

$${\xi_2}^{**} = m_0l_{-f} + m_f l_{-2f} + l_f m_{-2f} + l_0m_{-f}$$

$${\eta_1}^{**} = 2m_0l_1 + m_f l_{-f+1} + m_{-f} l_{f+1}$$

$${\eta_2}^{**} = m_{-f}l_1 + m_f l_{-2f+1} + m_{-2f}l_{f+1} + m_0l_{-f+1}$$

$${\zeta_1}^{*} = 4m_1m_1 + 2m_{1+f}m_{1-f} + 2m_{1+f}m_{1-f}$$

$$\zeta_2{}^{*}=2m_{1-f}m_1+2m_{1+f}m_{1-2f}+2m_{1-2f}m_{1+f}+2m_1m_{1-f}$$

$$\zeta_1{}^{*\prime}=4l_1l_1+2l_{1+f}l_{1-f}+2l_{1+f}l_{1-f}$$

$$\zeta_2{}^{*\prime}=2l_{1-f}l_1+2l_{1+f}l_{1-2f}+2l_{1-2f}l_{1+f}+2l_1l_{1-f}$$

$$\varsigma_1{}^{**}=2m_0l_2+m_fl_{2-f}+m_{-f}l_{f+2}$$

$$\varsigma_2{}^{**}=m_{-f}l_2+m_fl_{2-2f}+m_{-2f}l_{2+f}+m_0l_{2-f}$$

$$\zeta_1{}^{**}=4m_1l_1+2m_{1+f}l_{1-f}+2m_{1-f}l_{1+f}$$

$$\zeta_2{}^{**}=2m_{1-f}l_1+2m_{1-2f}l_{1+f}+2m_{1+f}l_{1-2f}+2m_1l_{1-f}$$

$$\vartheta_1{}^{**}=\varsigma_1{}^{**}+\zeta_1{}^{**}$$

$$\vartheta_2{}^{**}=\varsigma_2{}^{**}+\zeta_2{}^{**}$$

For each mode, the first three moments have the following relationships:

$$N_m=M_0 \qquad N_l=L_0 \tag{11a}$$

$$v_{mg}=\frac{M_1^2}{M_0^{3/2}M_2^{1/2}} \qquad v_{lg}=\frac{L_1^2}{L_0^{3/2}L_2^{1/2}} \tag{11b}$$

$$\ln^2\delta_{mg}=\frac{1}{9}ln\frac{M_0M_2}{M_1^2} \qquad \ln^2\delta_{lg}=\frac{1}{9}ln\frac{L_0L_2}{L_1^2} \tag{11c}$$

Through solving the first three moments, the particle number concentration, and the particle average diameter and its standard geometric deviation can be obtained, respectively. In the present study, the basic idea of the first three order moments of the method is used according to [20, 34].

Similarly, the dimensionless equation of the sulfuric acid molecular concentration is given as:

$$\frac{\partial \eta}{\partial t^*} = R^* - J^*(\upsilon^*)k^* - M_{2/3}^*\eta \tag{12a}$$

$$\frac{\partial \eta}{\partial t^*} = R^* - J^*(\upsilon^*)k^* - L_{2/3}^*\eta \tag{12b}$$

where η represents the concentration of molecular sulfuric acid, $R^* = R/(n_s/\tau)$ is the particle generation rate and k^* is the number of sulfuric acid containing in the critical particle. The dimensionless solution is identical to that in [2].

2.3 Computational detail and simulation setup

Since the particles are smaller than 1μm and the particle concentration is smaller than 0.1% by vol (m^3/m^3), the influence of particle phase on the flow field can be neglected and a single-phase on the flow field could be used. Thus, the large eddy simulation (LES) with standard wall function is used in the present study to model the flow field in the planar jet. In the work of [42], this combination of turbulence model and near-wall treatment was found to give the best agreement with experimental data. Simulations were carried out in two dimensions under the hypothesis of axial symmetry. A sketch of the reactor and of the computational domain used in the numerical simulations is shown in Fig. 1(a). Several grids are tested in order to verify that the solution is grid-independent, and it is found that a grid with 400 nodes in the radial direction and 500 nodes in the axial direction for a total of 200,000 computational cells is well justified for the present study. The present numerical simulation is performed in the two-dimensional computational domain as shown in Fig. 1(b), which is a planar jet flow where the x-axis and y-axis are the flow direction and the cross-stream direction, respectively. The spray nozzle width, W is set to be 5mm, and the size of flow direction and cross-stream direction is taken as $20W \times 40W$. The inlet carrier gas consisting of sulfuric acid and water vapor is injected to the aerosol reactor with the exhaust jet Reynolds number ranging from 2,000 to 5,000. Before the injection of carrier gas, the aerosol reactor contains uniformly distributed the background particles at 400K. The initial conditions of Mode 1 particles are presented in Case 1 of Table 2. The time-step, Δt is 1×10^{-4} s, and time, t is treated by $T = t/(W/U_0)$ for non-dimensionalization. In the present study, the SIMPLE scheme for pressure-velocity coupling and second order implicit transient formulation are used to solve the governing equations of fluid flow. The bounded central difference method is used for solving convective term in Eq. (2).

Fig. 1. A sketch of the reactor and of the computational domain: (a) the three-dimensional reactor configuration; (b) the two-dimensional computational domain.

In the present study, the B-TEMOM is implemented with the third-order Taylor-series expansion and the first three moments in Mode 1 and Mode 2 for a total of 6 moments are tracked. This choice is justified where the order of Taylor-series expansion equals to 3 was found to be the best configuration in terms of accuracy and computational costs [43]. Hence, the transport equations for the six moments are implemented.

The computational procedures are as follows:

First, the flow field is solved by the transient computing scheme until a fully developed flow state is reached. The convergence criteria required that all normalized residuals be smaller than 10^{-6}.

Next, the three moments of Mode 1 represent the background particles, their initial values are set to be uniform throughout the computational domain and the value could be found in Table 2 while the three moments of Mode 2 represent the generated particles, their initial values are set to be zero throughout the whole computational fluid domain. The convergence criteria for all scalars required that the normalized residuals be smaller than 10^{-6}.

The dimensionless scalar represents the sulfuric acid and water vapor concentration which is defined at the inlet and is initiated with a fixed value of 1,000. The numerical simulation scheme is transient and the time step is set to be 0.0001s.

3 Results and Discussion

3.1 Velocity field

Based on the experimental results obtained from [44], jet velocity profile in the cross section should satisfy the Gaussian normal distribution, which can be written as:

$$\frac{u}{u_m} = \exp\left(-\frac{y^2}{w^2}\right) \tag{13}$$

Theoretically, the streamwise velocity profile in the cross section should satisfy the self-similar distribution with the minimum of $x = 6.8W$. In the present study, the numerical simulation results in Fig. 2 show that when $x \geq 8W$, the streamwise velocity begins to satisfy the Gaussian normal distribution, which indicates that the jet flow of the present numerical simulation is close to both experimental and theoretical results.

Fig. 2. Self-similar normalized jet centerline velocity profiles at different *y* positions.

3.2 Instantaneous analysis

3.2.1 Particle number concentration

In the turbulent flow field, the evolution of the large coherent structures involves the temporal and spatial evolution of the particles. For the two-phase flow system of nanoparticles, the key physical properties concerned are the particle number density, the particle mass concentration, the particle polydispersity, and the average particle diameter. In the instantaneous analysis of the key physical properties of particles, the present study is focused on the near nozzle exit region, where the dynamic characteristics of the particles experience great changes. The Reynolds number of the exhaust jet, Re_j used for Figs 3 to 9 is around 2,000 with the jet injection velocity of 6.0 m/s and temperature 400K. Figs. 3 and 4 show the instantaneous contour of the jet particle number concentration M_0 and the jet particle number concentration L_0 generated by homogeneous nucleation at different non-dimensional times. As shown in Fig. 4, in the interface between the jet flow and the surrounding environment, the particle number concentration L_0 is relatively high, while in the jet centerline, $L_0$is almost zero. This implies that for the water and sulfuric acid vapor near the nozzle exit region, the binary homogeneous nucleation only occurs at the edge of the jet. In the downstream of the near nozzle exit region, the strong mixing between the jet flow and the background gas leads to the rapid decrease of the particle number concentrationL_0in the interface region.

However, the increase of the particle number concentration L_0 downstream of the jet centerline can be attributed to two reasons: first, particles formed on the edge region of the jet are entrained into the inner layer of the eddy by the coherent structures; second, the formation of new particles in the central part also increases the particle number density. Despite the increase of L_0 downstream of the jet centerline, the particle number concentration in the edge of downstream mixing region is still higher than the inner regions of large coherent structures, which is due to the high nucleation rate at the edge of the eddy and the effect of particle coagulation in the inner layer of the eddy. In the strong mixing region, the particle number concentration maintains the same characteristics as the large coherent structures.

Fig. 3. The instantaneous contour of jet particle number concentration, M_0 of Mode 1 at Re_j = 2,000 and dimensionless time (a) $T = 12$, (b) $T = 72$, (c) $T = 144$ and (d) $T = 240$.

Fig. 4. The instantaneous contour of jet particle number concentration, L_0 of Mode 2 at Re_j = 2,000 and dimensionless time (a) $T = 12$, (b) $T = 72$, (c) $T = 144$ and (d) $T = 240$.

3.2.2 Particle mass concentration

Fig.5 shows the instantaneous contour of particle mass concentration L_1 at different times. It can be observed that L_1 is largely the same as the distribution of particle number concentration L_0 in the near nozzle exit region, and higher particle mass concentration only exists at the edge of the jet near the nozzle exit. The downstream particle mass concentration of the central region of the coherent structures gradually increases along the axial x direction, but it is still less than the value at the edge region of the coherent structures. This phenomenon can be explained by the particle transfer from Mode 2 to Mode 1 as the flow develops in the axial direction, x. Over time, the maximum value of particle mass concentration also increases from 4.5×10^{-5} at $T=12$ to 5×10^{-3} (s/s) at $T=240$, which can be attributed to the longer relaxation time, the relatively higher nucleation and coagulation rates at the edge of the jet near the nozzle exit region.

Fig. 5. The instantaneous contour of jet particle mass concentration, L_1 of Mode 2 at Re_j = 2,000 and dimensionless time (a) $T = 12$, (b) $T = 72$, (c) $T = 144$ and (d) $T = 240$.

3.2.3 Particle polydispersity

In the developed B-TEMOM [6], the moment L_2 represents the particle polydispersity of Mode 2. Under the influence of coagulation, condensation and particle transfer from Mode 2 and Mode1, the polydispersity of small particles in Mode 2 increases significantly with time. Fig.6 shows the instantaneous contour evolution of L_2 with increasing time, i.e., $T = 12$ to $T = 240$. As shown in Fig. 6, the maximum value almost occurs at the edge of the jet flow near the nozzle exit region, which increases rapidly from 1.6×10^{-4} at $T = 12$ to 1.4×10^{-2} at $T = 240$. In the central region of the near nozzle exit, L_2 is almost near zero (i.e., there is almost no particle in this region), which is consistent with the L_0 contour in Fig.2. In the downstream of the jet flow, the value of L_2 is less than that in the near nozzle exit region, which may be observed because of larger particles in the process of particle transfer to the Mode1 (i.e., the range of large particles), leading to the decrease of particle polydispersity to the downstream of the jet flow

Fig. 6. The instantaneous contour of jet particle polydispersity, L_2 of Mode 2 at Re_j = 2,000 and dimensionless time (a) $T = 12$, (b) $T = 72$, (c) $T = 144$ and (d) $T = 240$.

3.2.4 Average particle diameter

In the present study, the only reason for the formation of particles is the existence of binary homogeneous nucleation. With the downstream development of the jet flow field, the variation of the particle size results from the binary homogeneous nucleation, coagulation and the condensation on the surface of large particles. Fig. 7 shows the distribution of average particle diameter, d_{lp}, which is similar to the distribution of L_0. But the distribution of d_{lp} in the flow field is also affected by the large coherent structures. The average particle diameter in the inner region of the large coherent structures is significantly smaller than that at the edge of the jet. This is because particles in the inner region have longer relaxation time for coagulation and condensation processes, and they will be adsorbed on the surface of the large particles as well. Thus, the average particle diameter in Mode1 in the inner region of the jet is smaller than that at the edge of the jet flow.

Fig. 7. The instantaneous contour of average particle diameter, d_{lp} (nm) of Mode 2 at Re_j = 2,000 and dimensionless time (a) $T = 72$, (b) $T = 144$, (c) $T = 240$ and (d) $T = 480$.

3.2.5 Fully developed jet flow and time-averaged results for the studied moments

Fig. 8(a) shows a fully developed jet flow, which demonstrates that the particle number concentration in the downstream is larger than the near nozzle exit region. In the downstream mixed region between jet flow and background gas, the value of L_0 is larger than the centerline region. However, when the jet flow is developed at the initial stage such as $T = 72$, $T = 240$ and $T = 480$, the particle number concentration, L_0 in the upstream mixed region is larger than the downstream region. This could contribute to a longer relaxation time of particles and a slower flow velocity, so the accumulation effect of particles gradually plays an important role.

Fig. 8. Contour of jet particle number concentration, L_0 in the fully developed jet flow at $Re_\mathrm{j} = 2{,}000$ and T=1,200.

3.2.6 Contour of time-averaged L_0 and d_p

Fig.9 (a) shows the time-averaged results of the particle number concentration, L_0 which is generated by the binary sulfuric and water molecule nucleation. When the jet flow is fully developed, 3,000 time steps are performed. Each time step is fixed to 0.0001s to obtain the time-averaged results. Compared with the instantaneous results in Fig. 8, it can be inferred that the binary nucleation rate is high in the near nozzle exit region due to a longer residence time caused by the existence of large eddy coherent structures. Similar results regarding the effect of larger coherent structures can also be found in [45-47]. A maximum particle number concentration is thus observed in downstream of the jet as shown in Fig 9(a). Fig. 9 (b) shows the contour of time-averaged average particle diameter. Large average particle diameter can be found in the near nozzle exit region, which is caused by two reasons. Firstly, the concentration of sulfuric acid and water and nucleation rate are very high in the near nozzle exit region. Secondly, the average particle diameter gradually increases because of the aerosol dynamic processes including coagulation, coalescence and surface growth, which increase the diameter of particles. However, if the average particle diameter exceeds a critical value, the governing mode will transfer from Mode 2 (for nucleated small particles) to Mode 1 (for large background particles). The longer relaxation time of large particles results in more and more particle transferring to the Mode 1. Thus, a smaller nucleation rate and average particle diameter can be found in the near centerline region of the downstream jet.

Fig. 9. Contour of (a) time-averaged jet particle number concentration, L_0 and (b) average particle diameter, d_{lp} (nm) for $Re_\mathrm{j} = 2{,}000$.

3.2.7 Different Reynolds numbers

In the unsteady flow study, the time-averaged results can be used to describe the key parameters statistically. The effects of different Reynolds numbers, Re_j on the particle number concentration are investigated for four simulation cases.

Fig. 10 shows the distributions of time-averaged particle number concentration, L_0 at $x = 0.01$ m, 0.02 m and 0.03 m in the y direction for different jet Reynolds numbers, Re_j. For the distribution of L_0 at $x = 0.01$ m as shown in Fig. 10 (a), the particle number concentration, L_0 increases significantly with increasing Re_j from 2,000 to 5,000. The results can be explained by the strengthening mixing effect in the near nozzle exit region caused by the increasing Re_j, which results in more particles generated by the homogenous nucleation. However, for the distributions of L_0 at x = 0.02 m and x = 0.03 m as shown in Figs. 10b and 10c, the results are just opposite, i.e., L_0 decreases significantly with increasing Re_j from 2,000 to 5,000. It may be caused by the lower jet flow velocity and higher relaxation time for the positions at x = 0.02 m and 0.03 m because the particles are larger at longer axial distance, x. The numerical simulation results obtained by the developed B-TEMOM [6] are further compared with those obtained by the sectional method (SM) [48]. Excellent agreement can be found for the studied cases with increasing jet Reynolds number, Re_j ranging from 2,000 to 5,000 and axial distance from 0.01 m to 0.03 m. The results validate the reliability and accuracy of B-TEMOM which indicate that this method is capable of capturing the spatial distributions of particle number concentrations in turbulent flows.

Fig.10. Comparison between the radial distributions of particle number concentration, L_0: (a) x = 0.01 m, (b) x = 0.02 m and (c) x = 0.03 m for different jet Reynolds numbers, Re_j by using B-TEMOM and the sectional method (SM) [48].

3.2.8 Comparison of time-averaged L_0 and d_p for different background conditions

The simulation parameters of the studied cases at Re_j= 2,000 for different background conditions are shown in Table 2. The studied Cases 1, 2 and 3 show different average particle diameter d_{mp} with the same initial number concentration M_0, whereas studied Cases 1, 4 and 5 show different initial number concentration M_0 with the same particle diameter d_{mp}. Fig. 11

shows the profile of time-averaged L_0 and d_{lp} in the y direction. In Fig. 11a, the diffusion of particles to the environment dilutes the particle number concentration L_0 along the downstream of the jet flow. Comparing the profiles of d_{mp} with the studied Cases 1, 2 and 3 in Fig. 11a, they show that the background of average particle diameter d_{mp} partially influences the particle number concentration L_0 generated by binary nucleation. Comparing the profiles of d_{mp} with the studied Cases 1, 4 and 5 in Fig. 8b, they show a significant decrease in the particle number concentration L_0 with the initial particle number concentration M_0 increasing by an order of magnitude sequentially, especially for high M_0**.** This finding can be attributed to the behavior that when the newly generated particles grow to a certain size, they will be automatically divided into Mode 1, which is further enhanced by the increasing M_0. However, according to Figs. 11(c) and 11(d), the variation of key parameters (i.e., particle number concentration, M_0 and average particle diameter, d_{mp}) only has a very slight influence on the average particle diameter d_{lp}. Although the results show that the average particle diameter of the newly generated particles will be limited to a certain size, they can be adsorbed on the surface of larger particles in Mode 1 if they grow to a sufficient size. This shows that the existing background particles can inhibit the growth and limit the particle number concentration of the newly generated particles.

Table 2 The simulation parameters of the studied cases used in the time-average analysis for Re_j= 2,000.

Fig. 11. Cross-stream profiles of $Re_j = 2{,}000$ (a-b) jet particle number concentration, L_0 and (c-d) average particle diameter, d_{lp} (nm) for studied Cases 1-2-3 and Cases 1-4-5 at $x = 0.05$ m, respectively.

4. Conclusions

In the present study, the developed bimodal Taylor-series expansion method of moments (B-TEMOM) for the GDEs of nanoparticles is coupled with the large eddy simulation (LES) method. The LES method is used in conjunction with the method of moments in the numerical simulation of a planar nanoparticle-gas jet flow in both the spatial and temporal domains. The results of the velocity distribution show excellent agreement with the self-preserving distribution. The instantaneous and time-averaged PSDs are obtained. This approach provides a better prediction of the evolution of bimodal particulate flow and the effect of the large coherent structures on the nanoparticle dynamics.

The distributions of the number concentration, mass concentration, polydispersity and average diameter of particles are found to be similar to the large coherent structures. The number concentration, mass concentration, polydispersity and average diameter of particles are greatly affected by the large coherent structures, causing enhanced particle dispersion due to the dilution effect. By using this B-TEMOM, it can be found that the key physical parameters of the newly generated particles by binary homogeneous nucleation is significantly affected by the particle transfer between these two modes. The number concentration, mass concentration, polydispersity and average diameter of particles in the central region of the jet flow field downstream can all be attributed to the existing large size particle mode. The time-averaged information of the different studied cases was within the fully developed flow region. In comparing the cross-stream profiles of the particle number concentration, L_0 and average particle diameter, d_{lp} for studied Cases 1, 2 and 3, and studied cases 1, 4 and 5 at $x = 0.05$ m, the particle number concentration in Mode 2 is greatly influenced by the particle number concentration of Mode1. It is also demonstrated that the background particles can prohibit the growth of the newly generated particles. The numerical simulation results obtained by the B-TEMOM are further validated with those obtained by the sectional method with excellent agreement. The results in the present study also show that this developed B-TEMOM can be further used to solve more practical and complex aerosol-related problems, such as heavy metal emission problems, vehicle exhaust problems, dust removal, etc., which can be treated as a bimodal distribution model.

5. Acknowledgements

This work was supported by grants from the General Research Fund, Research Grants Council of the Hong Kong Special Administrative Region, China (Project No. PolyU 5101/13E) and the Central Research Grant of The Hong Kong Polytechnic University (Project Nos. B-Q39E and G-YBF5).

References

[1] W.J. Stark, S.E. Pratsinis, Aerosol flame reactors for manufacture of nanoparticles, Powder Technology 126(2002) 103-108.

[2] S.E. Pratsinis, Simultaneous nucleation, condensation, and coagulation in aerosol reactors, Journal of Colloid and Interface Science 124(1988) 416–427.

[3] D. Lee, & M. Choi, Coalescence enhanced synthesis of nanoparticles to control size, morphology and crystalline phase at high concentrations, Journal of Aerosol Science 33(2002) 1–16.

[4] J.I. Jeong, M. Choi, A bimodal particle dynamics model considering coagulation, coalescence and surface growth, and its application to the growth of Titania aggregates, Journal of Colloid and Interface Science 281(2005) 351–359.

[5] Y.H. Liu, H. Gu, The Taylor-expansion method of moments for the particle system with bimodal distribution, Thermal Science 17(2013) 1542-1545.

[6] M.Z. Yu, T.L. Chan, A bimodal moment method model for submicron fractal-like agglomerates undergoing Brownian coagulation, Journal of Aerosol Science 88 (2015) 19–34.

[7] S.R. Lee, C.Y. Wu, Size distribution evolution of fine aerosols due to inter-coagulation with coarse aerosols, Aerosol Science and Technology 39(2005) 358–370.

[8] M. Jonasz, F. Georges, Approximation of the size distribution of marine particles by a sum of log-normal functions, Limnology and Oceanography 41(1996) 744–754.

[9] C.H. Jung, Y.P. Kim, K.W. Lee, A moment model for simulating raindrop scavenging of aerosols, Journal of Aerosol Science 34(2003) 1217–1233.

[10] F.Y. Yuan, F.J. Gan, Evolution of aerosol particles in the rainfall process via method of moments, Abstract and Applied Analysis 2013(2013) 1–7.

[11] S.K. Friedlander, Smoke, dust and haze: Fundamentals of aerosol behavior (2nd Ed.), John Wiley & Sons, Inc., 2000.

[12] J.D. Landgrebe, S.E. Pratsinis, A discrete-sectional model for particulate production by gas-phase chemical reaction and aerosol coagulation in the free-molecular regime, Journal of Colloid and Interface Science 139(1990) 63–86.

[13] D. Mitrakos, E. Hinis, C. Housiadas, 2007. Sectional modeling of aerosol dynamics in multi-dimensional flows, Aerosol Science and Technology 41 (2007) 1076-1088.

[14] P. Agarwal, S.L. Girshick, Sectional modeling of nanoparticle size and charge distributions in dusty plasmas, Plasma Sources Science and Technology 21(2012) 055023.

[15] M. Frenklach, Method of moments with interpolative closure, Chemical Engineering Science 57(2002) 2229–39.

[16] H.M. Hulburt, S. Katz, Some problems in particle technology, Chemical Engineering Science 19(1964) 555–574.

[17] K.W. Lee, H. Chen, J.A. Gieseke, Log-normally preserving size distribution for Brownian coagulation in the free-molecule regime, *Aerosol Science and Technology* 3(1984) 53–62.

[18] D. L. Marchisio, R.D. Vigil, R.O. Fox, Quadrature method of moments for aggregation-breakage processes, Journal of Colloid and Interface Science 258(2003) 322–334.

[19] R. McGraw, Description of aerosol dynamics by the quadrature method of moments, Aerosol Science and Technology 27(1997) 255–65.

[20] M.Z. Yu, J.Z. Lin, T.L. Chan, A new moment method for solving the coagulation equation for particles in Brownian motion. Aerosol Science and Technology 42(2008) 705–713.

[21] Y.K. Park, S.C. Jung, S.H. Park, Development of a moment model for condensational obliteration of nanoparticle aggregates, Journal of Nanoscience and Nanotechnology 13(2013) 2008-2011.

[22] Z.L. Chen, J.Z. Lin, M.Z Yu, Direct expansion method of moments for nanoparticle Brownian coagulation in the entire size regime, Journal of Aerosol Science 67(2014) 28-37.

[23] M. Pollack, S. Salenbauch, D.L. Marchisio, C. Hasse, Bivariate extensions of the extended quadrature method of moments (EQMOM) to describe coupled droplet evaporation and heat-up, Journal of Aerosol Science 92(2016) 53-69.

[24] M. Kraft, Modelling of particulate processes, Kona 23(2005) 18–35.

[25] H.B. Zhao, C.G. Zheng, A population balance-monte carlo method for particle coagulation in spatially inhomogeneous systems, Computers & Fluids 71(2013) 196–207.

[26] S.Y. Liu, T.L. Chan, A stochastically weighted operator splitting Monte Carlo (SWOSMC) method for the numerical simulation of complex aerosol dynamic processes, International Journal of Numerical Methods for Heat & Fluid Flow 27(2017) 263-278.

[27] S.Y. Liu, T.L. Chan, A coupled CFD-Monte Carlo method for aerosol dynamics in turbulent flows, Aerosol Science and Technology 51(2017) 269-281.

[28] D.L. Marchisio, R.O. Fox, Solution of population balance equations using the direct quadrature method of moments, Journal of Aerosol Science 36(2005) 43–73.

[29] R.O. Fox, F. Laurent, M. Massot, Numerical simulation of spray coalescence in an Eulerian framework: direct quadrature method of moments and multi-fluid method, Journal of Computational Physics 227(2008) 3058–3088.

[30] M.E. Mueller, G. Blanquart, H. Pitsch, Hybrid method of moments for modeling soot formation and growth, Combustion and Flame 156(2009) 1143–55.

[31] T.L. Chan, Y.H. Liu, C.K. Chan, Direct quadrature method of moments for the exhaust particle formation and evolution in the wake of the studied ground vehicle, Journal of Aerosol Science 41(2010) 553–568.

[32] C. Yuan, R.O. Fox, Conditional quadrature method of moments for kinetic equations, Journal of Computational Physics 230(2011) 8216–8246.

[33] C. Yuan, F. Laurent, R.O. Fox, An Extended quadrature method of moments for population balance equations, Journal of Aerosol Science 51(2012) 1–23.

[34] M.Z. Yu, J.Z. Lin, Taylor-expansion moment method for agglomerate coagulation due to Brownian motion in the entire size regime, Journal of Aerosol Science 40(2009) 549–62.

[35] C.M. Megaridis, R.A. Dobbins, A bimodal integral solution of the dynamic equation for an aerosol undergoing simultaneous particle inception and coagulation, Aerosol Science and Technology 12(1990) 240-255.

[36] E.R. Whitby, P.H. McMurry, Modal aerosol dynamics modeling, Aerosol Science and Technology 27(1997) 673–688.

[37] M. Frenklach, S.J. Harris, Aerosol dynamics modelling using the method of moments, Journal of Colloid and Interface science 118(1987) 252-261.

[38] M.Z. Yu, Y.H. Liu, M. Seipenbusch, 0P TEMOM scheme for solving the population balance equation, Aerosol Science and Technology 49(2015) 1021–1036.

[39] P. Lau, M. Kind, CFD-PBE simulation to predict particle growth in a fluidized bed melt granulation batch process, Powder Technology 300(2016) 28-36.

[40] C.D. Immanuel, F.J. Doyle, Solution technique for a multi-dimensional population balance model describing granulation processes, Powder Technology 156 (2005) 213-225.

[41] M.Z. Yu, J.Z. Lin, T. Chan, Numerical Simulation of Nanoparticle Synthesis in Diffusion Flame Reactor, Powder Technology 181 (2008) 9-20.

[42] D.L. Marchisio, A.A. Barresi, M. Garbero, Nucleation, growth and agglomeration in barium sulphate turbulent precipitation, A.I.Ch.E. Journal 48(2002) 2039–2050.

[43] M.Z. Yu, X.T. Zhang, Y.H. Liu, M. Seipenbusch, Verification of expansion orders of the Taylor-series expansion method of moment model for solving population balance equations, Aerosol and Air Quality Research 15(2015) 2475-2484.

[44] W. Forstall, A.H. Shapiro, Momentum and mass transfer in coaxial gas jets, American Society of Mechanical Engineers-Transactions-Journal of Applied Mechanics 18(1951) 219–220.

[45] K. Zhou and T.L. Chan*, Simulation of Homogeneous Particle Nucleation in a Free Turbulent Jet. Aerosol Science and Technology 45(2011)) 973-987.

[46] J.Z. Lin, T.L. Chan*, S. Liu, K. Zhou, Y. Zhou and S.C. Lee, Effects of Coherent Structures on Nanoparticle Coagulation and Dispersion in a Round Jet. International Journal of Nonlinear Sciences and Numerical Simulation 8(2007) 45-54.

[47] T.L. Chan*, J.Z. Lin, K. Zhou, and C.K. Chan, Simultaneous Numerical Simulation of Nano and Fine Particle Coagulation and Dispersion in a Round Jet. Journal of Aerosol Science 37(2006) 1545-1561.

[48] S. Tsantilis, H. K. Kammler, S. E. Pratsinis, Population balance modeling of flame synthesis of Titania nanoparticles. Chemical Engineering Science, 57(2002) 2139-2156.

List of Figures

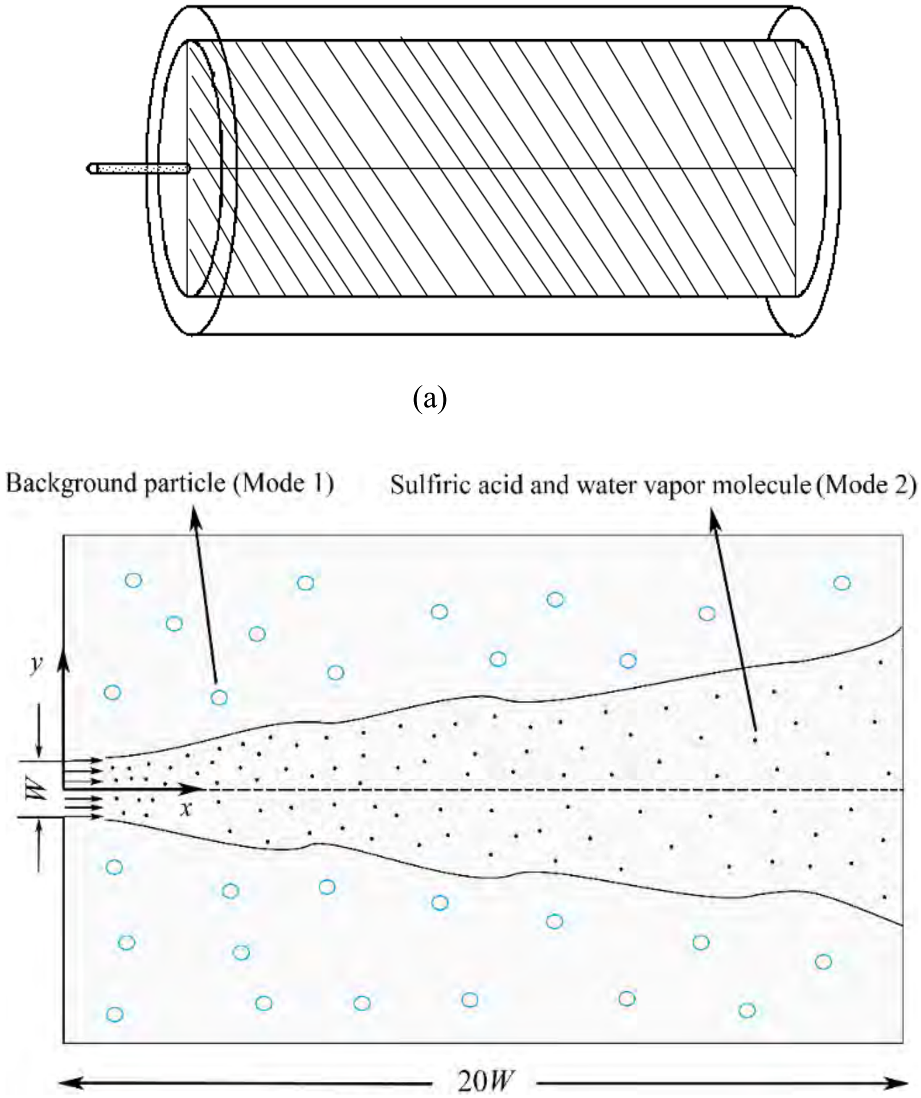

(a)

(b)

Fig. 1. A sketch of the reactor and of the computational domain: (a) the three-dimensional reactor configuration; (b) the two-dimensional computational domain.

.

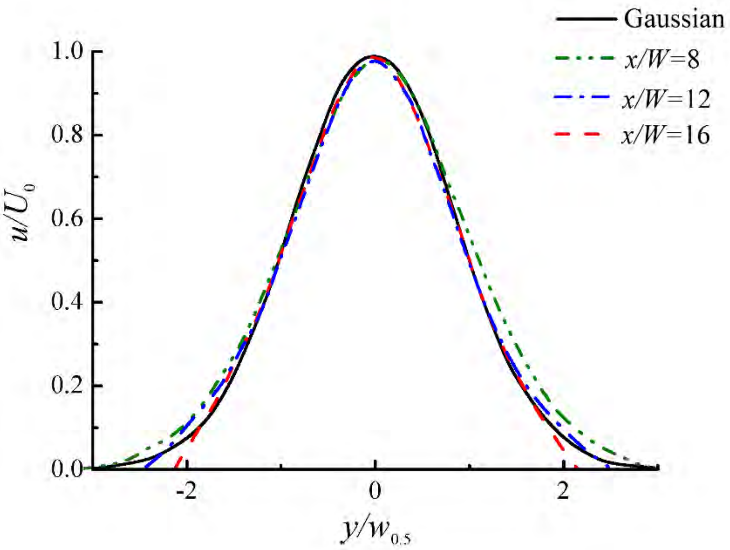

Fig. 2. Self-similar normalized jet centerline velocity profiles at different y positions.

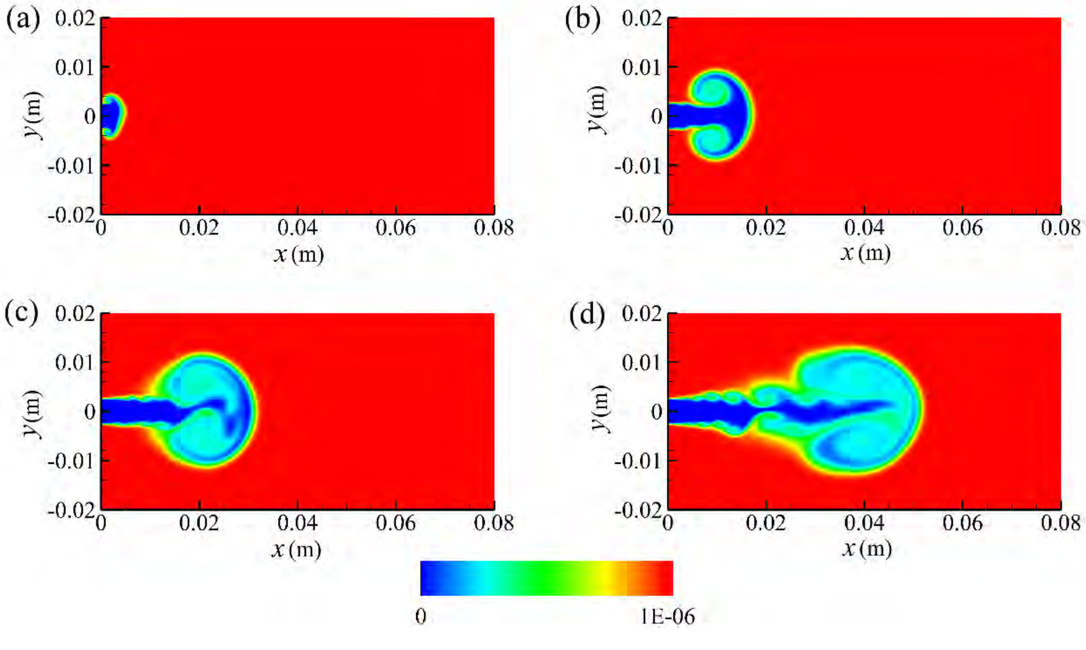

Fig. 3. The instantaneous contour of the jet particle number concentration, M_0 of Mode 1 at Re_j = 2,000 and dimensionless time (a) T = 12, (b) T = 72, (c) T = 144 and (d) T = 240.

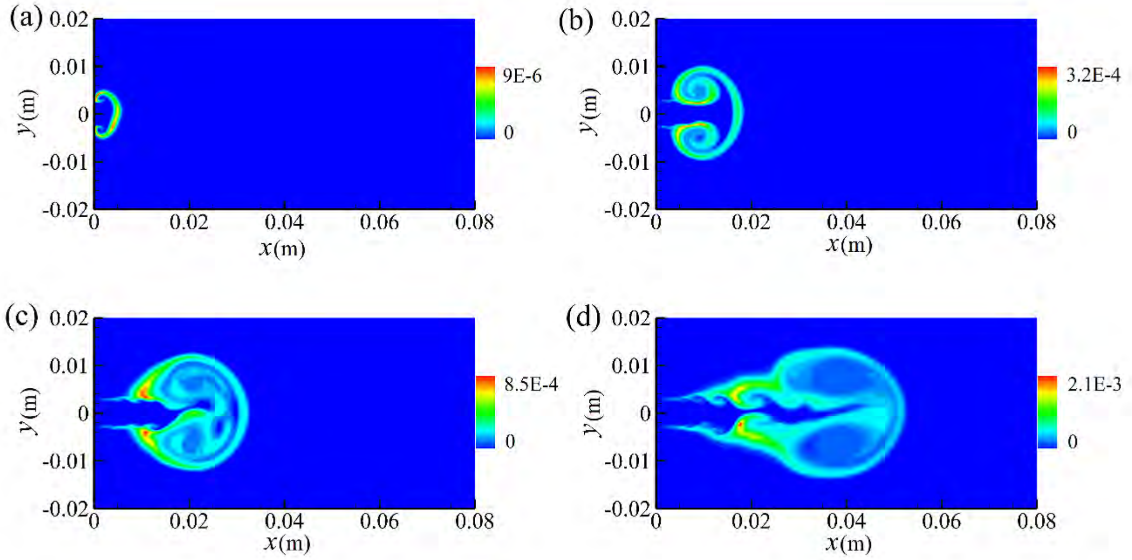

Fig. 4. The instantaneous contour of jet particle number concentration, L_0 of Mode 2 at at Re_j = 2,000 and dimensionless time (a) T =1 2, (b) T = 72, (c) T = 144 and (d) T = 240.

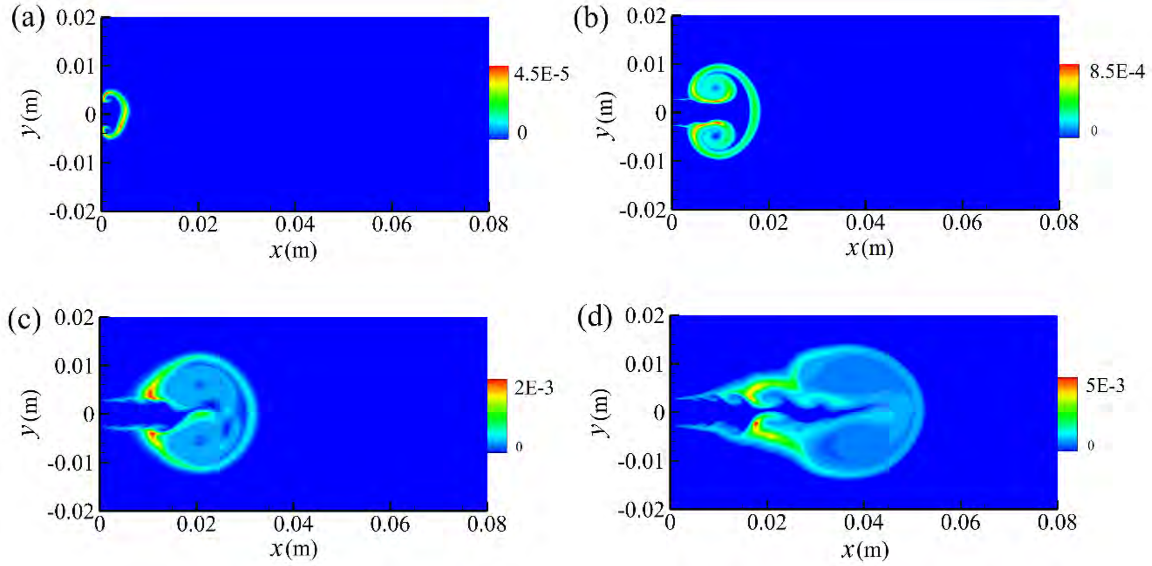

Fig. 5. The instantaneous contour of jet particle mass concentration, L_1 of Mode 2 at Re_j = 2,000 and dimensionless time (a) T = 12, (b) T = 72, (c) T = 144 and (d) T = 240.

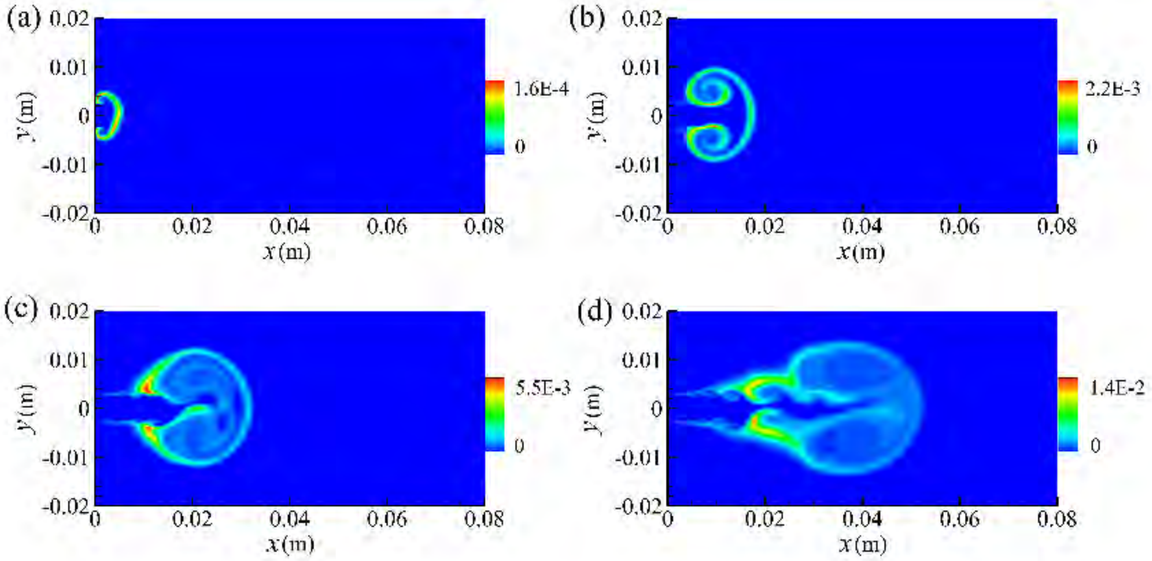

Fig. 6. The instantaneous contour of jet particle polydispersity, L_2 of Mode 1 at $Re_j = 2{,}000$ and dimensionless time (a) $T = 12$, (b) $T = 72$, (c) $T = 144$ and (d) $T = 240$.

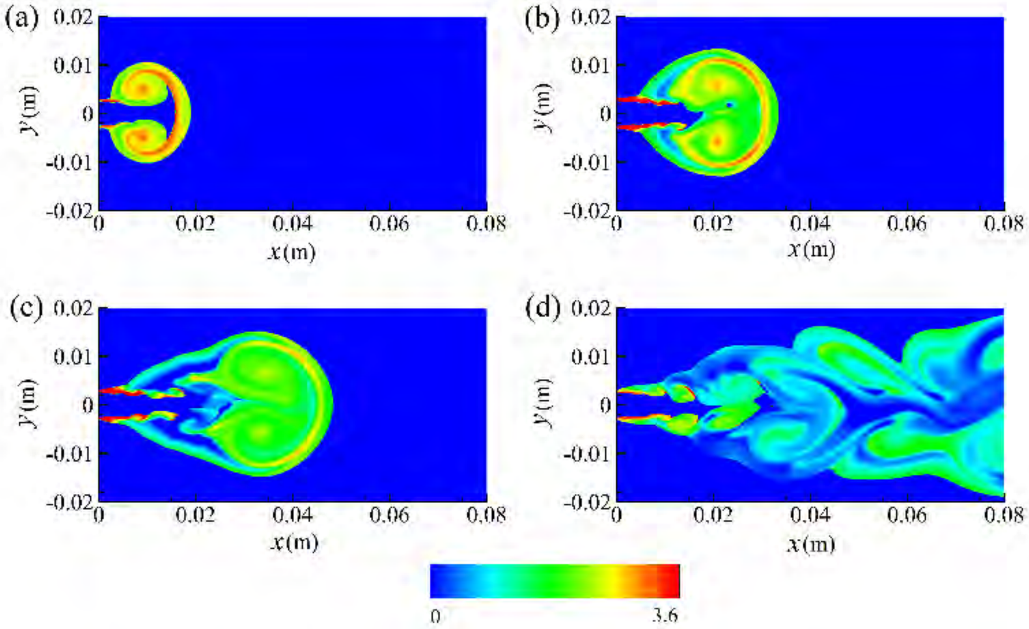

Fig. 7. The instantaneous contour of average particle diameter, d_{lp} (nm) of Mode 2 at $Re_j = 2{,}000$ and dimensionless time (a) $T = 72$, (b) $T = 144$, (c) $T = 240$ and (d) $T = 480$.

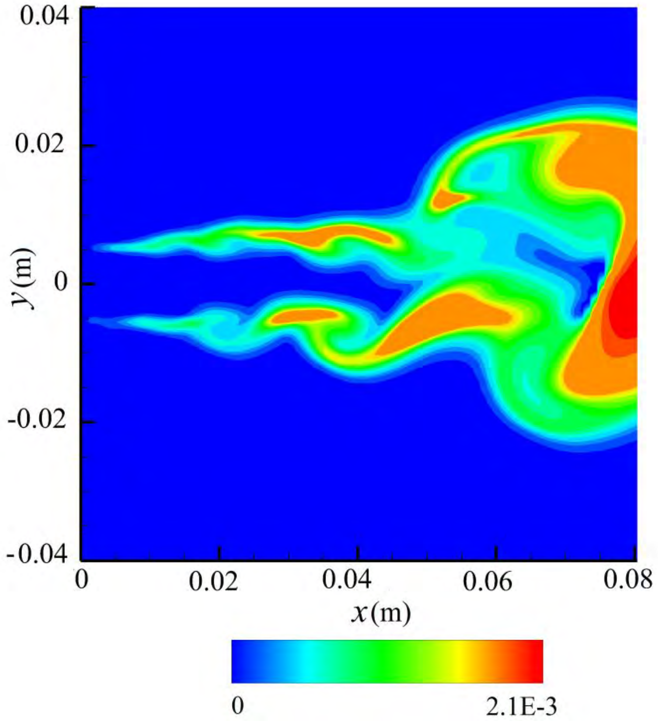

Fig. 8. Contour of jet particle number concentration, L_0 in fully developed jet flow at $Re_j = 2,000$ and $T = 1,200$.

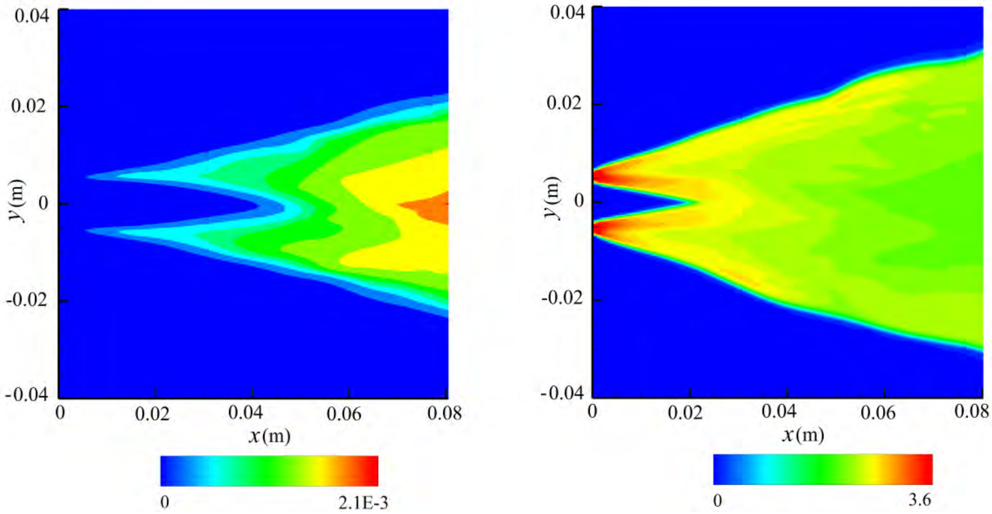

(a) (b)

Fig. 9. Contour of (a) time-averaged jet particle number concentration, L_0 and (b) average particle diameter, d_{lp} (nm) for $Re_j = 2,000$.

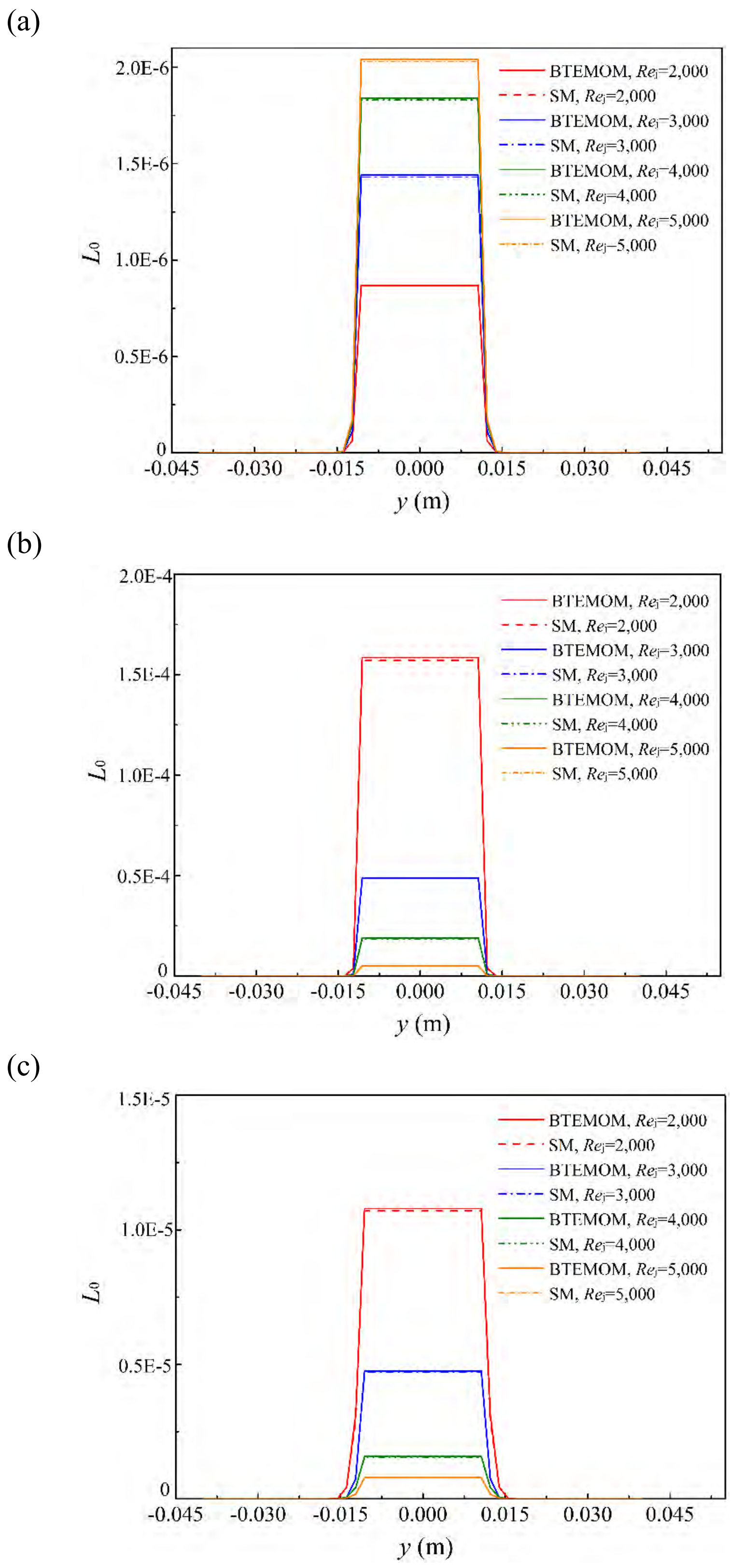

Fig. 10. Comparison between the radial distributions of particle number concentration, L_0: (a) $x = 0.01$ m, (b) $x = 0.02$ m and (c) $x = 0.03$ m for different jet Reynolds numbers, Re_j by using B-TEMOM and the sectional method (SM) [48].

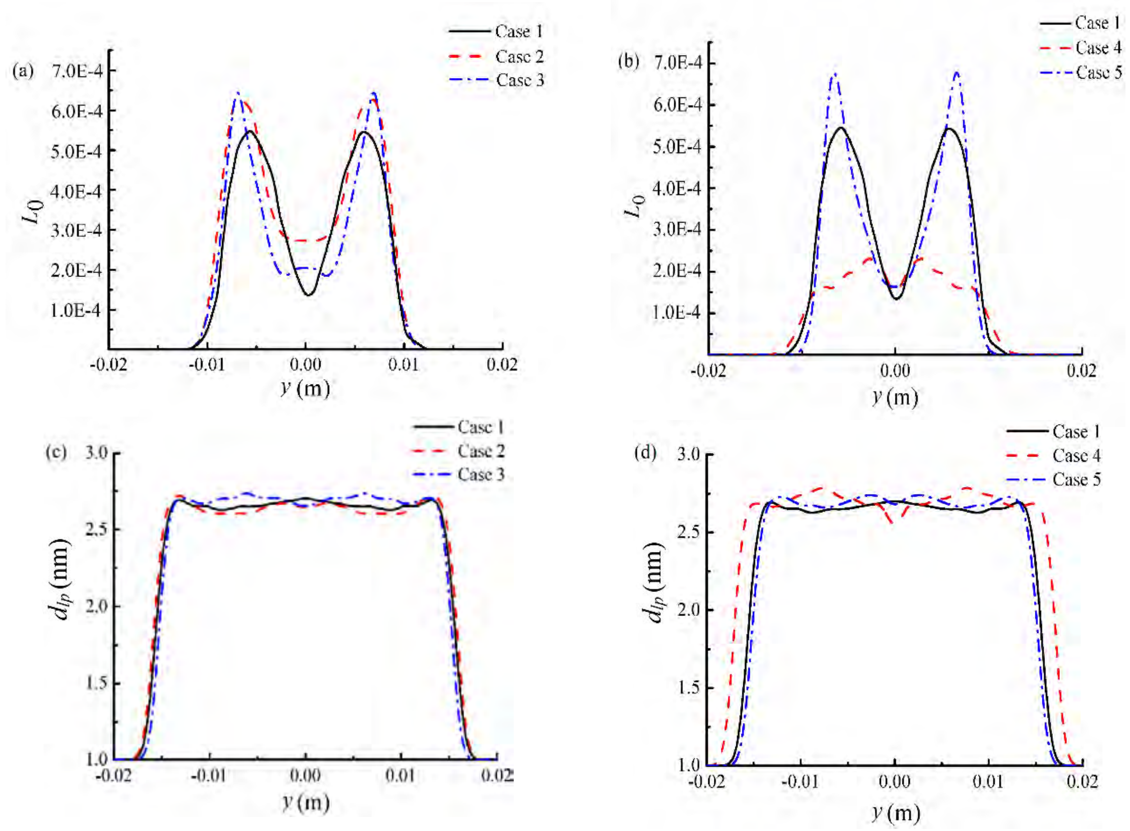

Fig. 11. Cross-stream profiles of Re_j = 2,000 (a-b) jet particle number concentration, L_0 and (c-d) average particle diameter, d_{lp} for studied Cases 1-2-3 and Cases 1-4-5 at x = 0.05 m, respectively.

List of Tables

Table 1 Non-dimensional terms used in the present study.

Terms	Meaning
$\tau=1/[n_s s_1 (k_b T_k/2\pi m_a)^{1/2}]$	Characteristic time, where s_1 is the surface area of sulfuric acid molecules, n_s is the reference concentration of sulfuric acid molecule in gas phases, m_a is the molecular mass of sulfuric acid, k_b is Boltzmann constant, T_k is temperature.
$t^*=t/\tau$	Dimensionless time.
$T = t/(W/U_0)$	Dimensionless time, W is the width of the nozzle, U_0 is the injection velocity of the jet.
$m_k^*=m_k/n_s\, v_a^k$	Dimensionless moments where v_a is the volume of sulfuric acid molecule, $v_a=v_{p0}$, m_k and l_k are the kth moments of large particles (Mode 1) and small particles (Mode 2), respectively.
$l_k^*=l_k/n_s\, v_a^k$	
$J^*(v^*)=\dfrac{J(v^*)}{n_s/\tau}$	Dimensionless nucleation rate.

Table 2 The simulation parameters of the studied cases used in the time-averaged analysis for $Re_j = 2{,}000$.

Cases	M_0	d_{mp} (nm)	δ_{mg}	m_0^*	m_1^*	m_2^*
1	5×10^{10}	100	1.60	1×10^{-6}	42.2	1.30×10^{10}
2	5×10^{10}	200	1.60	1×10^{-6}	338	8.33×10^{11}
3	5×10^{10}	500	1.60	1×10^{-6}	5280	2.04×10^{14}
4	5×10^{11}	100	1.60	1×10^{-5}	422	1.30×10^{11}
5	5×10^{9}	100	1.60	1×10^{-7}	4.22	1.30×10^{9}